

Facile ion-exchange synthesis of BiOI/Bi₂O₂CO₃ heterostructure for efficient photocatalytic activity under visible light irradiation

Cheng Liu · Bo Chai

Received: 22 September 2014 / Accepted: 9 January 2015 / Published online: 14 January 2015
© Springer Science+Business Media New York 2015

Abstract The BiOI/Bi₂O₂CO₃ heterostructural photocatalysts were synthesized by a facile ion-exchange route between Bi₂O₂CO₃ precursor and KI with ultrasonic reaction. The as-prepared BiOI/Bi₂O₂CO₃ heterostructures were characterized by X-ray diffraction (XRD), field emission scanning electron microscopy (FESEM), high-resolution transmission electron microscopy (HRTEM), X-ray photoelectron spectroscopy (XPS), UV–Vis diffuse reflectance absorption spectra (DRS), fourier transform infrared spectroscopy (FTIR) and photoluminescence spectra (PL). The BiOI/Bi₂O₂CO₃ heterostructures exhibited much higher photocatalytic activities than those of single Bi₂O₂CO₃ and BiOI for the degradation of Rhodamine B (RhB) under visible light irradiation. The significantly enhanced photocatalytic activity of BiOI/Bi₂O₂CO₃ heterostructures could be attributed to the formation of p–n heterojunction between p-type BiOI and n-type Bi₂O₂CO₃, which effectively separated the photogenerated electron–hole pairs. The possible mechanism of BiOI/Bi₂O₂CO₃ heterostructures as photocatalysts was proposed.

1 Introduction

Semiconductor photocatalysis driven by visible light has been a hot topic of intensive interest because of its potential applications in environmental decontamination and hydrogen energy production by utilization of solar light energy [1, 2]. In recent years, a large number of visible-light-responsive

photocatalysts have been explored, such as AgBr [3], Ag₃PO₄ [4], Ag₂CO₃ [5], BiVO₄ [6], Bi₂MoO₆ [7], Bi₂WO₆ [8], BiOBr [9], BiOI [10] and C₃N₄ [11]. Despite of above photocatalysts exhibit visible-light-responsive performances, the high recombination rate of photogenerated charge carriers and photocorrosion restrict their potential applications. Therefore, it is necessary to develop an efficient strategy toward improving the separation efficiency of photogenerated charge carriers, further extending visible light spectral responsive range and photostability. Recent investigations indicate that constructing heterostructural photocatalysts is one of the most promising ways to solve above issues [12–17]. For example, the novel heterostructural photocatalysts Ag–AgBr/TiO₂ [12], Ag₃PO₄/C₃N₄ [13], Cu₂O/BiVO₄ [14], Bi₂MoO₆/TiO₂ [15], Ag/AgBr/BiOBr [16], BiOBr/BiOI [17] have been developed to enhance the photocatalytic activities and stabilities comparing with the above single component photocatalysts.

Recently, bismuth compounds such as BiVO₄ [6], Bi₂MoO₆ [7], Bi₂WO₆ [8], Bi₂O₂CO₃ [18, 19], BiOX (X = Cl, Br, I) [20, 21] etc. have received more attention due to their excellent photocatalytic properties for the degradation of organic contaminations. Among these compounds, Bi₂O₂CO₃, as one member of the Aurivillius family of layered oxides, is composed of alternate Bi₂O₂²⁺ and CO₃²⁻ layers [18]. However, the wide band gap (2.87–3.58 eV) of single Bi₂O₂CO₃ restricts its practical application under visible light. Therefore, constructing Bi₂O₂CO₃-based heterostructure would become a feasible method to extend the spectral responsive range, improve the charge separation efficiency, and enhance the photocatalytic activity and stability of Bi₂O₂CO₃. Some Bi₂O₂CO₃-based heterostructural photocatalysts, including of BiVO₄/Bi₂O₂CO₃ [22], Bi₂WO₆/Bi₂O₂CO₃ [23], Bi₂MoO₆/Bi₂O₂CO₃ [24], Bi₂S₃/Bi₂O₂CO₃ [25], C₃N₄/Bi₂O₂CO₃ [26], Bi₂O₃/Bi₂O₂CO₃ [27] have been

C. Liu · B. Chai (✉)
School of Chemical and Environmental Engineering, Wuhan Polytechnic University, Wuhan 430023, People's Republic of China
e-mail: willycb@163.com

reported to be efficient for the degradation of organic contaminants under visible light irradiation. As another member of the Aurivillius family, BiOI composed of alternate $\text{Bi}_2\text{O}_2^{2+}$ and I^- layers has a narrow band gap about 1.80 eV, which make it absorb most of the visible light [10]. However, single BiOI usually showed poor photocatalytic activity due to the high recombination rates of photogenerated charge carriers. In order to improve the photocatalytic activity of BiOI, the BiOI-based composites have been explored such as BiOI/TiO₂ [28] and BiOI/ZnO [29]. In these cases, BiOI can serve as an efficient visible light photosensitizer for the wide band gaps TiO₂ or ZnO to greatly enhance their photocatalytic performances. Consequently, coupled BiOI with the wide band gap Bi₂O₂CO₃ to formation heterostructural photocatalysts may be an effective method to improve the photocatalytic activities of BiOI and Bi₂O₂CO₃. Additionally, in view of the fact that Bi₂O₂CO₃ and BiOI are similar in structure, they can easily grow together to form heterostructure. Cao et al. have synthesized the BiOI/Bi₂O₂CO₃ heterojunction photocatalysts by etching Bi₂O₂CO₃ precursor with hydroiodic acid (HI) solution. The BiOI/Bi₂O₂CO₃ hybrid showed much higher photocatalytic activity than pure Bi₂O₂CO₃ and BiOI for the degradation of MO under visible light illumination [30]. Yin et al. have fabricated the BiOI/Bi₂O₂CO₃ composites by a facile chemical co-precipitation method using Na₂CO₃ and NH₄I solution. The photocatalytic activity of BiOI/Bi₂O₂CO₃ is much higher than that of its components [31].

In this study, we have prepared the BiOI/Bi₂O₂CO₃ heterostructure by a facile partial ion-exchange method between Bi₂O₂CO₃ and KI with ultrasonic reaction at acidic condition. Because of the solubility difference, I^- ions could react with Bi₂O₂CO₃ to form BiOI on the Bi₂O₂CO₃. The photocatalytic activities of BiOI/Bi₂O₂CO₃ heterostructures prepared by controlling ultrasonic reaction time for the degradation of Rhodamine B (RhB) solution were investigated comparatively. The possible mechanism for enhanced photocatalytic activity was proposed based on the obtained experimental results.

2 Experimental

2.1 Material preparation

All chemicals are analytical grade reagents purchased from Sinopharm Chemical Reagent Co, Ltd. (SCRC) without further purification. The Bi₂O₂CO₃ precursors were prepared referred to previous reports [18]. Typically, 1 mmol Bi(NO₃)₃·5H₂O and 2 mmol tri-sodium citrate were added into 60 mL deionized water with stirring at room temperature. After stirring for 1 h, the pH value of the solution was adjusted to 9.0 by diluted NH₃·H₂O. After stirring for

another 1 h, the mixed solution was transferred into a 100 mL Teflon-lined stainless steel autoclave and kept at 180 °C for 24 h, and then cooled to room temperature naturally. The obtained products were collected using centrifugation and washed with deionized water and ethanol for several times, then dried at 80 °C overnight.

The BiOI/Bi₂O₂CO₃ heterostructures were synthesized through the ion-exchange method between Bi₂O₂CO₃ precursor and KI solution with ultrasonic reaction. The 0.1 g of as-prepared Bi₂O₂CO₃ was introduced into 10 mL 0.1 mol L⁻¹ KI solution, and the pH value of the mixed solution was adjusted to 1.0 with a certain concentration HNO₃ solution, followed the mixture was sonicated for different times. In this case, the obtained BiOI/Bi₂O₂CO₃ heterostructures with ultrasonic reaction times for 15, 30, 45, and 60 min were denoted as samples S1, S2, S3 and S4, respectively. For comparison, the single BiOI was prepared by adding 1 mmol KI to the 1 mmol Bi(NO₃)₃·5H₂O solution with sonication for 1 h. The products were centrifuged, washed with deionized water and ethanol for several times, and then dried at 80 °C for 12 h.

2.2 Material characterization

The products were characterized by XRD patterns using a Bruker D8 Advance X-ray diffractometer with Cu-K α irradiation ($\lambda = 0.154178$ nm) at 40 kV and 40 mA. The morphology of samples was investigated by a JSM-6700F microscope operation at 10 kV. The HRTEM measurement was conducted using a JEOL JEM 2100F microscope working at 200 kV. The XPS measurement was performed on a VG Multilab 2000 with Al-K α source operation at 300 W. The UV–Vis diffuse reflectance absorption spectra were obtained by a Shimadzu UV-3,600 spectrophotometer equipped with an integrating sphere using BaSO₄ as the reference sample. The FTIR spectra of samples were recorded on a Thermo Nicolet Avatar 360 spectrometer using conventional KBr pellets. The PL was measured at room temperature on a Varian Cary Eclipse fluorescence spectrophotometer with the excitation wavelength at 320 nm.

2.3 Photocatalytic activity measurement

The photocatalytic activities of as-prepared BiOI/Bi₂O₂CO₃ heterostructures were evaluated by degradation of RhB aqueous solution under visible light irradiation. The 30 mg of photocatalysts were added into 100 mL of RhB solution with the initial concentration of 2.0×10^{-5} mol L⁻¹. A 500 W tungsten halogen lamp was positioned inside a cylindrical Pyrex vessel and surrounded by a circulating water jacket (Pyrex) to cool the lamp. A cutoff filter was placed outside the Pyrex jacket to completely remove all wavelengths less than 420 nm to ensure the

irradiation with visible light only. Prior to irradiations, the suspensions were magnetically stirred in the dark for 30 min to ensure the establishment of an adsorption–desorption equilibrium. At given irradiation time intervals, 4 mL of the suspensions were collected and then the slurry samples including the photocatalysts and RhB solution were centrifuged (10,000 rpm, 10 min) to remove the photocatalysts. The TU-1,810 spectrophotometer was used to measure the concentration changes of RhB solution with the wavelength of 554 nm.

3 Results and discussion

XRD was used to investigate the phase structure of the obtained products. Figure 1 shows the XRD patterns of single $\text{Bi}_2\text{O}_2\text{CO}_3$, BiOI and BiOI/ $\text{Bi}_2\text{O}_2\text{CO}_3$ heterostructures. It is observed that all the diffraction peaks of BiOI can be indexed to tetragonal phase BiOI (JCPDS NO. 73-2,062) with well resolved (001), (002), (012), (110), (013), (004), (020), (114) and (122) reflections, which is in agreement with the literature [10]. No diffraction peak for any other crystal phase is detected, indicating that there is no crystal phase impurity existing in the obtained BiOI samples. Moreover, the intense diffraction peaks of the BiOI suggest that the as-prepared sample would be well crystallized. The peaks of $\text{Bi}_2\text{O}_2\text{CO}_3$ can be indexed to the standard XRD patterns of $\text{Bi}_2\text{O}_2\text{CO}_3$ (JCPDS NO. 41-1,488). However, the diffraction peaks of $\text{Bi}_2\text{O}_2\text{CO}_3$ are relatively broadened, which is due to lower crystallinity and the distortion of lattice. The phenomena are usually observed in the synthesis of microsphere-like $\text{Bi}_2\text{O}_2\text{CO}_3$ samples [18]. The BiOI/ $\text{Bi}_2\text{O}_2\text{CO}_3$ heterostructures (S1–S4) exhibit the coexistence of both $\text{Bi}_2\text{O}_2\text{CO}_3$ and BiOI phases. Moreover, with the increasing ultrasonic reaction times, the intensities of (012) and (110) planes of BiOI

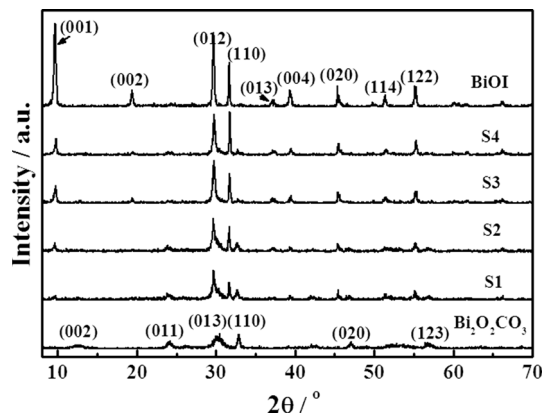


Fig. 1 XRD patterns of single $\text{Bi}_2\text{O}_2\text{CO}_3$, BiOI and BiOI/ $\text{Bi}_2\text{O}_2\text{CO}_3$ heterostructures (S1, S2, S3, S4)

obviously increase, whereas the characteristic planes of (013) and (110) of $\text{Bi}_2\text{O}_2\text{CO}_3$ decrease simultaneously, indicating that $\text{Bi}_2\text{O}_2\text{CO}_3$ transform gradually into BiOI to form the heterostructures.

Figure 2 shows the FESEM and TEM images of pristine $\text{Bi}_2\text{O}_2\text{CO}_3$ and S3 sample. As can be seen from Fig. 2a, the single $\text{Bi}_2\text{O}_2\text{CO}_3$ self-organized into microspheres with the average diameter of 2–3 μm . From an individual $\text{Bi}_2\text{O}_2\text{CO}_3$ microsphere, it can be found that the microsphere is comprised of massive interleaving nanosheets (inset in Fig. 2a) by close packing mode. As for the S3 sample, the densely packed microspheres turn into loose hierarchical structures and a large amount of lamelliform fragments as shown in Fig. 2b, indicating that the single $\text{Bi}_2\text{O}_2\text{CO}_3$ has partially transform into the BiOI. In the formation process of BiOI/ $\text{Bi}_2\text{O}_2\text{CO}_3$ heterostructure, BiOI can be in situ formed and intimately contact with the unreacted $\text{Bi}_2\text{O}_2\text{CO}_3$, which facilitates the charge carrier transfer and improves the photocatalytic activity. The TEM image of S3 sample shown in Fig. 2c also confirms that the S3 sample is constituted with some hierarchical structure (residual $\text{Bi}_2\text{O}_2\text{CO}_3$) and lamellar structure (BiOI), in accordance with FESEM observation. In the HRTEM image (Fig. 2d), the interplanar spacings are measured to be 0.19 and 0.30 nm, which can be assigned to the (020) plane of $\text{Bi}_2\text{O}_2\text{CO}_3$ and the (012) plane of BiOI, respectively. It is apparent that there are heterojunctions between $\text{Bi}_2\text{O}_2\text{CO}_3$ and BiOI in the as-prepared sample [31].

The XPS measurement was performed to determine the chemical composition and valence state of various species. The peak positions in all of the XPS spectra were calibrated with C 1 s at 284.6 eV. Figure 3a shows the XPS survey spectrum of S3 sample. As expected, it contains Bi, C, O and I elements. The peaks (Fig. 3b) with binding energy of 159.2 and 164.5 eV in the high resolution XPS spectrum of Bi 4f are ascribed to Bi 4f_{7/2} and Bi 4f_{5/2}, indicating the main chemical state of Bi in the sample is +3 [32]. The satellite peaks with a distance of 2.0 eV away from Bi 4f_{7/2} and Bi 4f_{5/2} main peaks are accorded with the reported values [28]. The O 1 s XPS spectrum illustrated in Fig. 3c can be deconvoluted into three peaks at 529.8, 531.1 and 532.2 eV, which correspond to the Bi–O bonds in [Bi_2O_2] slabs, carbonate species and –OH bonds of the surface adsorbed water, respectively [32]. As shown in Fig. 3d, the high resolution C 1 s spectrum can be fitted with two peaks. The peak located at 284.6 eV is usually assigned to adventitious carbon, another weak peaks positioned at 288.8 eV is corresponded to carbonate ion in $\text{Bi}_2\text{O}_2\text{CO}_3$ [32]. As for the high resolution I 3d XPS spectrum (Fig. 3e), two peaks at 618.7 and 630.2 eV are associated with I 3d_{5/2} and I 3d_{3/2}, respectively, in good agreement with those in BiOI [30]. The XPS results further prove the coexistence of $\text{Bi}_2\text{O}_2\text{CO}_3$ and BiOI in the S3 sample.

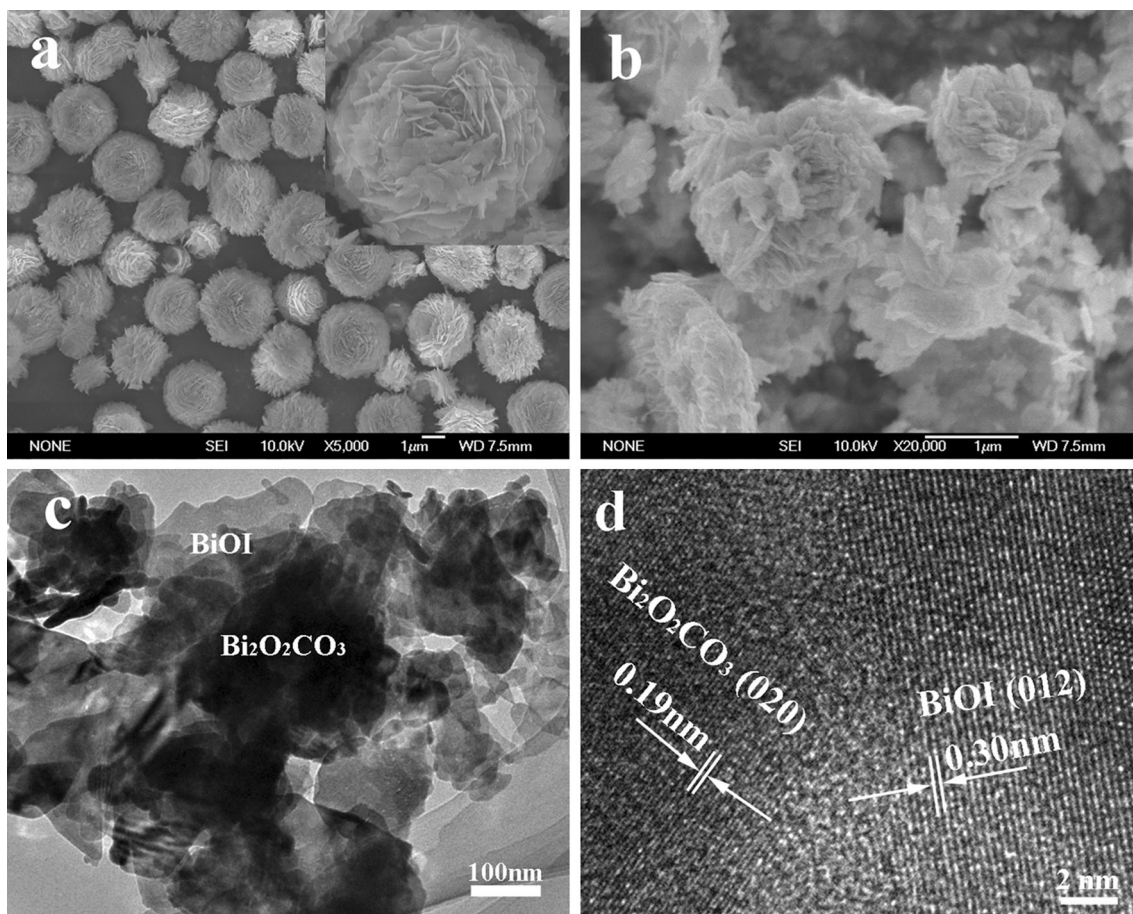


Fig. 2 FESEM images of pure $\text{Bi}_2\text{O}_2\text{CO}_3$ (an individual $\text{Bi}_2\text{O}_2\text{CO}_3$ microsphere, *inset*) **a** and S3 sample **b**; TEM **c** and HRTEM **d** images of S3 sample

Figure 4 shows the UV–Vis diffuse reflectance absorption spectra of pure $\text{Bi}_2\text{O}_2\text{CO}_3$, BiOI and S3 sample. As can be seen, $\text{Bi}_2\text{O}_2\text{CO}_3$ presents a steep absorption edge at about 380 nm. The bare BiOI has strong absorption in visible light region, with an absorption edge around 670 nm. The absorption spectrum of S3 sample exhibits a similar curve to that of BiOI, suggesting that the formation of BiOI/ $\text{Bi}_2\text{O}_2\text{CO}_3$ heterostructure can extend the spectral responsive range comparing with the single $\text{Bi}_2\text{O}_2\text{CO}_3$, and then improve the utilization of visible light.

The band gap energy of a semiconductor can be calculated by the following formula [30]:

$$\alpha hv = B(hv - E_g)^{n/2} \tag{1}$$

where α , h , v , E_g , and B are optical absorption coefficient, Planck’s constant, light frequency, band gap energy, and a constant, respectively. Among them, the value of n depends on the type of optical transition in a semiconductor ($n = 1$ for direct transition and $n = 4$ for indirect transition). As for $\text{Bi}_2\text{O}_2\text{CO}_3$ and BiOI, the values of n are both 4 for the indirect transition of them [30]. Therefore, the band gap

energy could be estimated by a related curve of $(\alpha hv)^{1/2}$ versus photon energy (hv) plotted from the intersection of the extrapolated linear portion (Fig. 4b). The estimated band gap energies of $\text{Bi}_2\text{O}_2\text{CO}_3$, BiOI and S3 sample were approximately 3.26, 1.80 and 1.84 eV, respectively.

Figure 5 depicts the FTIR spectra of single $\text{Bi}_2\text{O}_2\text{CO}_3$, BiOI and S3 sample. The broad peaks at about $3,420\text{ cm}^{-1}$ in all of the spectra correspond to the stretching vibration mode of $-\text{OH}$, and the physically adsorbed H_2O also contributes to this broad peak. For pure $\text{Bi}_2\text{O}_2\text{CO}_3$, the peaks at $1,386$ and $1,467\text{ cm}^{-1}$ are assigned to the anti-symmetric vibration mode of the CO_3^{2-} group, the peak at 846 cm^{-1} is related to out-of-plane bending vibration mode of the CO_3^{2-} [32]. The peak at 548 cm^{-1} is ascribed to the stretching vibration of Bi–O bond in $\text{Bi}_2\text{O}_2\text{CO}_3$ [30]. As for BiOI, the peaks about at $1,628$ and 489 cm^{-1} are attributed to the $-\text{OH}$ bending vibration of adsorbed H_2O molecules and Bi–O band stretching vibration in BiOI [30]. In the case of the S3 sample, the characteristic bands for $\text{Bi}_2\text{O}_2\text{CO}_3$ still remain, new peaks emerge at $1,628$ and 489 cm^{-1} , which are attributed to the featured peaks of

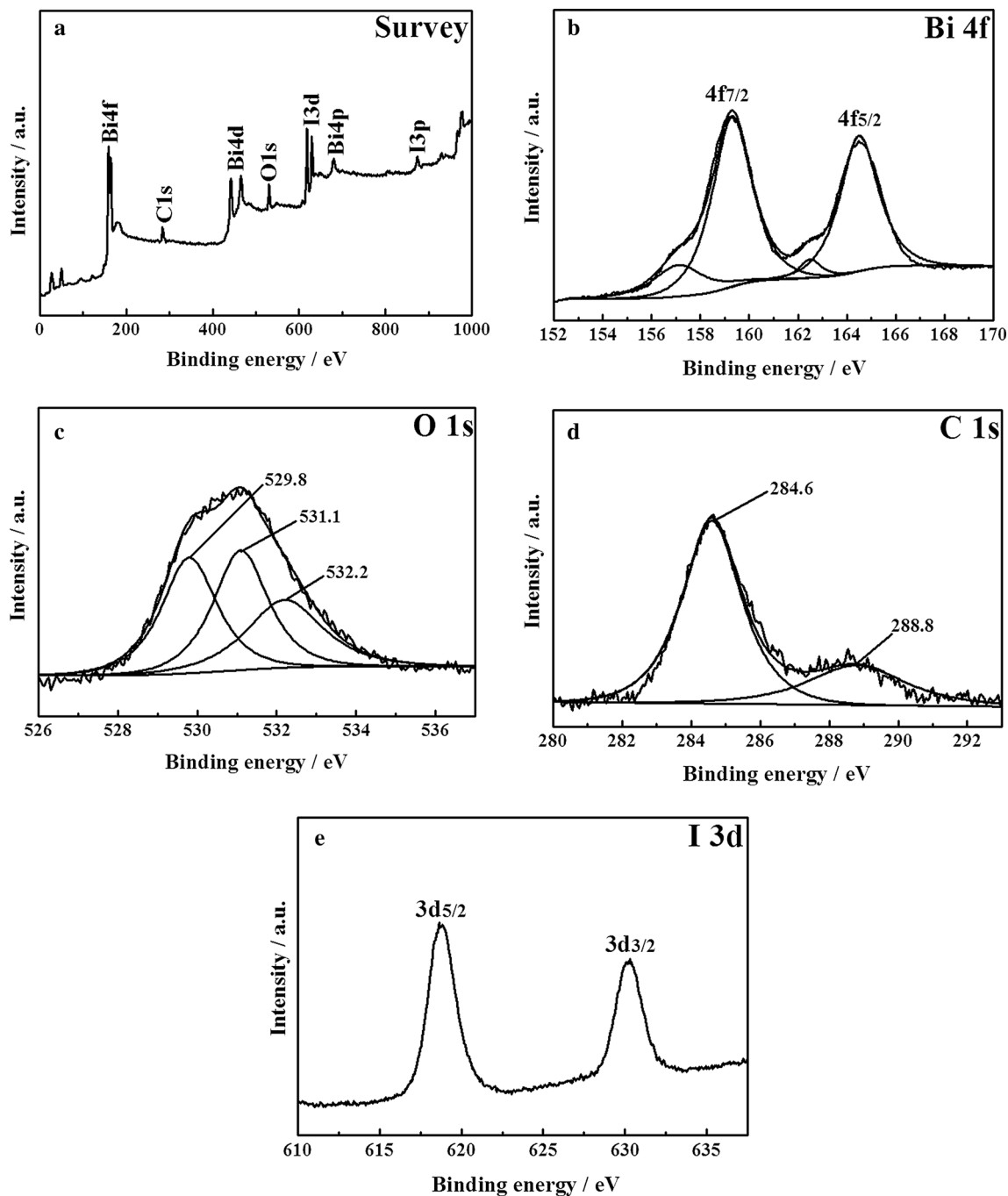


Fig. 3 XPS spectra of S3 sample: **a** XPS survey spectrum; **b** high resolution Bi 4f spectrum; **c** high resolution O 1 s spectrum; **d** high resolution C 1 s spectrum; **e** high resolution I 3d spectrum

BiOI, proving the $\text{Bi}_2\text{O}_2\text{CO}_3$ and BiOI coexistence in the S3 sample.

Figure 6 displays the photocatalytic activities of different catalysts for the degradation of RhB solution. RhB is a common model compound to test the photodegradation capability of catalyst. For comparison, the blank test was also conducted under the same reaction conditions. It could be seen that the degradation percentage of RhB is very low

in the absence of photocatalysts under visible light irradiation for 90 min. The single $\text{Bi}_2\text{O}_2\text{CO}_3$ and BiOI exhibit poor photocatalytic activities with the degradation percentages of 6.6 and 19.5 % after 90 min visible light irradiation, respectively. Since $\text{Bi}_2\text{O}_2\text{CO}_3$ can not respond to visible light, the degradation process is ascribed to dye-sensitized photocatalysis. On the other hand, the lower degradation efficiency of BiOI may be attributed to fast

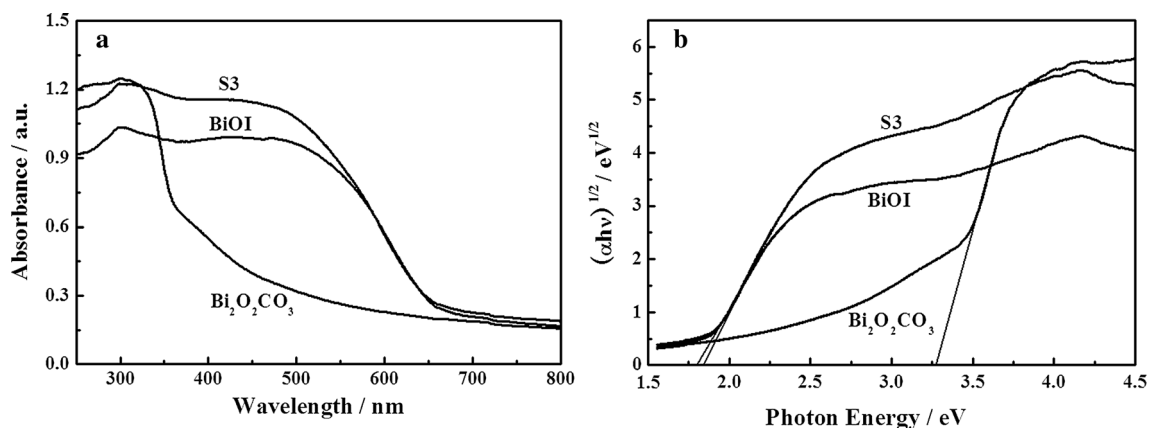


Fig. 4 UV-Vis diffuse reflectance absorption spectra of pure Bi₂O₂CO₃, BiOI and S3 sample (a) and plots of the $(\alpha h\nu)^{1/2}$ versus photon energy ($h\nu$) for the Bi₂O₂CO₃, BiOI and S3 sample (b)

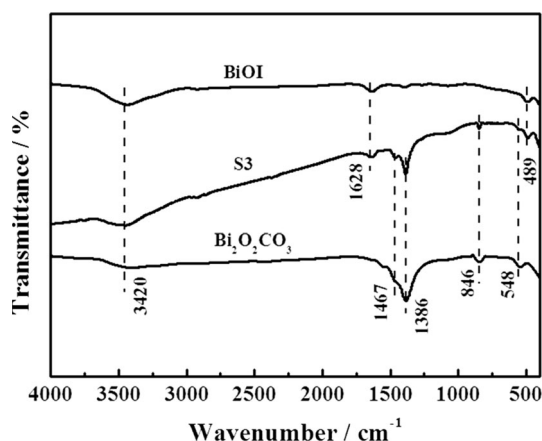


Fig. 5 FTIR spectra of pure Bi₂O₂CO₃, BiOI and S3 sample

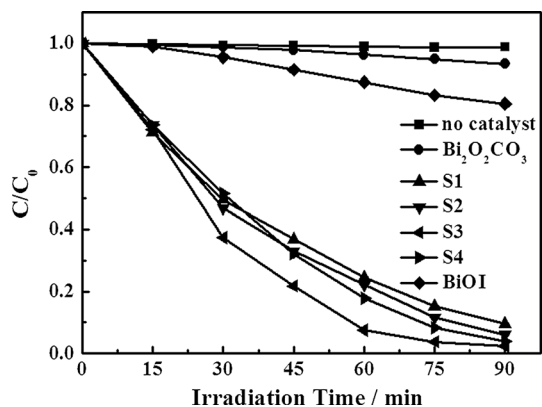


Fig. 6 Comparison of photocatalytic activities of the samples for the degradation of RhB solution

recombination of photogenerated electron-hole pairs of BiOI with narrow band gap. It is worth noting that the BiOI/Bi₂O₂CO₃ heterostructures greatly enhance the photocatalytic activity. After 90 min visible light irradiation, the photocatalytic degradation percentages of RhB are

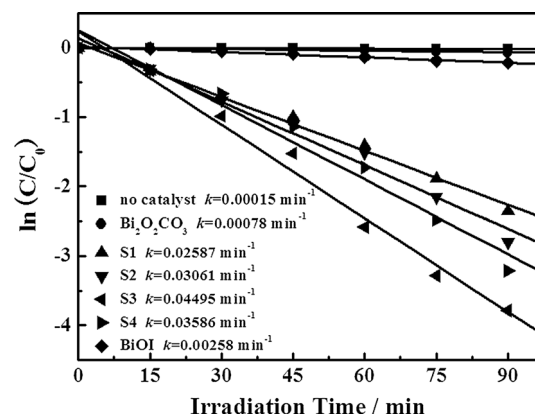


Fig. 7 Pseudo-first-order kinetics curves of RhB degradation over different samples

about 90.5, 93.9, 97.8 and 96.0 % for S1, S2, S3 and S4 samples, respectively. The results indicate that the formation of BiOI/Bi₂O₂CO₃ heterostructures facilitates the separation of photoinduced charge carriers and enhance the photocatalytic activity.

Generally, the photocatalytic degradation of RhB could be considered as a pseudo-first-order reaction with low concentration, and its kinetics could be expressed as follows:

$$-\ln(C/C_0) = kt \tag{2}$$

where k is the degradation rate constant, C_0 and C are the absorption equilibrium concentration of RhB and the concentration of the pollution at a reaction time of t , respectively. As shown in the Fig. 7, the rate constants (k) of different samples are 0.00078, 0.02587, 0.03061, 0.04495, 0.03586, 0.00258 and 0.00015 min⁻¹ for pure Bi₂O₂CO₃, S1, S2, S3, S4, BiOI and without catalyst, respectively. As for a series of BiOI/Bi₂O₂CO₃ heterostructural photocatalysts, the photocatalytic activity of heterostructures enhance with increasing ultrasonic reaction time and the S3

sample (sonication for 45 min) shows the highest photocatalytic performance. However, prolonging sonication time for 60 min, the photocatalytic activity of BiOI/Bi₂O₂CO₃ heterostructure decrease, which is due to the formation of excessive BiOI content in the composites and leading to the decrease of heterojunction interface [30]. For the degradation of RhB, the photocatalytic degradation efficiency of S3 composite is about 57.6 and 17.4 times higher than those of pure Bi₂O₂CO₃ and BiOI, respectively.

To test the stability and reusability of BiOI/Bi₂O₂CO₃ heterostructures for the photocatalytic reaction, the sample of S3 was reused for photocatalytic reaction four times under the same conditions, and the result is shown in Fig. 8. The photocatalytic efficiency of S3 composite still reaches 87.3 % after four recycled photocatalytic reaction. The results suggest that BiOI/Bi₂O₂CO₃ heterostructure has a good photostability.

To make the reaction mechanism clear, isopropanol (IPA), triethanolamine (TEOA) and p-benzoquinone (BQ) were respectively introduced as the scavengers of hydroxyl radicals ($\cdot\text{OH}$), holes (h^+) and superoxide radicals ($\cdot\text{O}_2^-$) to examine the effects of reactive species on the photocatalytic degradation of RhB. The concentrations of IPA, TEOA and BQ in the reaction system were 10, 10 and 1 mmol L⁻¹, respectively. In Fig. 9, we can see that the TEOA and BQ lead to a remarkable suppression of the degradation rate of RhB. The IPA exhibits a weaker restraining effect on the degradation rate. The results indicate that h^+ and $\cdot\text{O}_2^-$ play the more important role than $\cdot\text{OH}$ in the photocatalytic degradation of RhB.

Based on the above results, the enhanced photocatalytic activity of BiOI/Bi₂O₂CO₃ composite could be attributed to the heterojunction structure between BiOI and Bi₂O₂CO₃. It is generally accepted that the photogenerated electrons and holes transfer to the surface to react with the adsorbed reactants, and the migration direction of photo-generated charge carrier depends on the band edge position

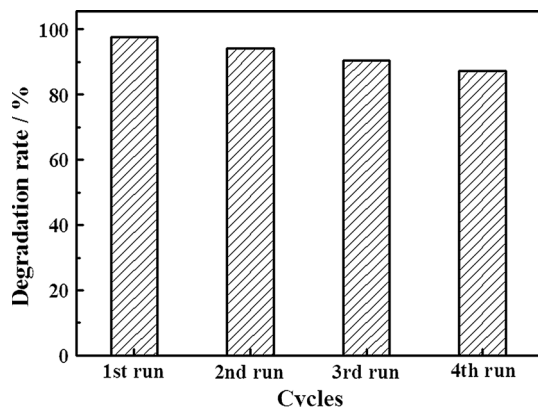


Fig. 8 Stability study of photocatalytic degradation of RhB over S3 sample

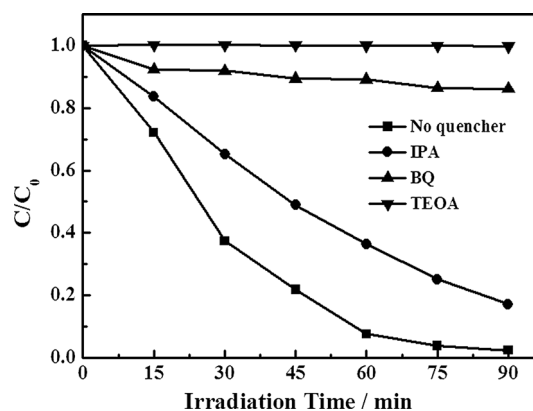


Fig. 9 The effect of reactive species on the photocatalytic degradation of RhB over S3 sample

of semiconductors. The conduction band (CB) and valence band (VB) potential of BiOI and Bi₂O₂CO₃ are calculated by the following equations [30]:

$$E_{VB} = X - E^e + 0.5E_g \quad (3)$$

$$E_{CB} = E_{VB} - E_g \quad (4)$$

where E_{VB} is the VB edge potential, E_{CB} is the CB edge potential, X is the electronegativity of semiconductor, which is the geometric mean of the electronegativity of the constituent atoms, E^e is the energy of free electrons on the hydrogen scale (about 4.5 eV). The X value of BiOI and Bi₂O₂CO₃ are ca. 5.94 and 6.35 eV, and the top of VB and the bottom of CB of BiOI are calculated to be 2.34 and 0.54 eV, respectively. According to the above equations, the VB and CB of Bi₂O₂CO₃ are estimated to be 3.48 and 0.22 eV, respectively. The energy band structure diagram of BiOI and Bi₂O₂CO₃ is schematically illustrated in Fig. 10a. Based on previous reports [30, 31], BiOI is a p-type semiconductor whose Fermi energy level is located close to the VB, whereas Bi₂O₂CO₃ is a n-type semiconductor whose Fermi energy level lies close to the CB. When BiOI is in contact with Bi₂O₂CO₃ to form a p–n

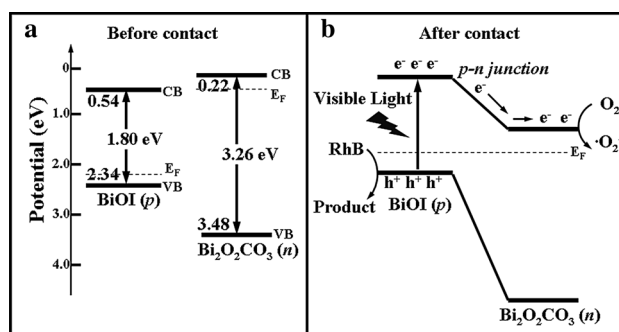


Fig. 10 Schematic diagrams of **a** energy band of Bi₂O₂CO₃ and BiOI before contact and **b** the formation of p–n junction and the proposed charge separation process

junction, the electrons diffuse from $\text{Bi}_2\text{O}_2\text{CO}_3$ into BiOI, resulting in an accumulation of negative charges in the BiOI region close to the junction. At the same time, the holes transfer from BiOI to $\text{Bi}_2\text{O}_2\text{CO}_3$, leaving a positive section in $\text{Bi}_2\text{O}_2\text{CO}_3$ near the junction. With equilibration of BiOI and $\text{Bi}_2\text{O}_2\text{CO}_3$ Fermi energy levels, an internal electric field is simultaneously built to stop the charge diffusion. Meanwhile, the energy bands of $\text{Bi}_2\text{O}_2\text{CO}_3$ shift downward along with the Fermi energy level, whereas those of BiOI shift upward in the process (Fig. 10b). Under visible light irradiation, BiOI can be easily excited and induce the generation of electron and hole pairs. According to the schematic diagram in Fig. 10b, the excited electrons on CB of p-type BiOI effectively transfer to that of n-type $\text{Bi}_2\text{O}_2\text{CO}_3$ under the effect of internal electric field and then react with O_2 adsorbed on the surface of catalysts to produce reactive species $\cdot\text{O}_2^-$. Following the oxidative species $\cdot\text{OH}$ is produced in the reaction of $\cdot\text{O}_2^-$ with photogenerated electrons. However, the VB potential of BiOI is higher than that of $\text{Bi}_2\text{O}_2\text{CO}_3$, thus the photogenerated holes remain on the surface of BiOI and directly oxidize RhB. In this case, the formation of p–n heterojunction (BiOI/ $\text{Bi}_2\text{O}_2\text{CO}_3$) could effectively separate the photoexcited electron–hole pairs and remarkably reduce the recombination of photogenerated charge carriers. As a result, the BiOI/ $\text{Bi}_2\text{O}_2\text{CO}_3$ heterostructures exhibit better photocatalytic activity than those of single $\text{Bi}_2\text{O}_2\text{CO}_3$ and BiOI for the degradation of RhB under visible light irradiation.

The better separation of photogenerated electrons and holes in the BiOI/ $\text{Bi}_2\text{O}_2\text{CO}_3$ heterostructures is confirmed by PL emission spectra of $\text{Bi}_2\text{O}_2\text{CO}_3$, BiOI and S3 sample. It is well known that the PL signals of semiconductor materials result from the recombination of photoinduced charge carriers. In generally, the lower PL intensity indicates the decrease in recombination rate of photogenerated charge carriers. As shown in Fig. 11, $\text{Bi}_2\text{O}_2\text{CO}_3$ exhibits an intense emission peak at about 370 nm, which is ascribed

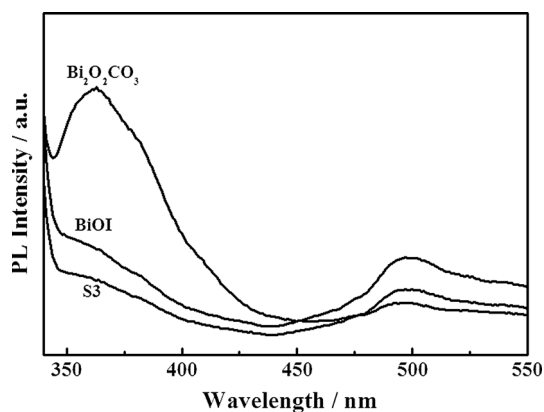


Fig. 11 PL emission spectra of $\text{Bi}_2\text{O}_2\text{CO}_3$, BiOI and S3 sample

to the emission of band gap transition. Compared with that of $\text{Bi}_2\text{O}_2\text{CO}_3$, the emission peak intensity of S3 sample decrease considerably, indicating that the recombination of photogenerated charge carriers is inhibited extremely. The result of PL verifies that the BiOI/ $\text{Bi}_2\text{O}_2\text{CO}_3$ heterostructures could most effectively separate photogenerated electron–hole pairs.

4 Conclusions

In summary, the BiOI/ $\text{Bi}_2\text{O}_2\text{CO}_3$ heterostructures synthesized via a facile ion-exchange route with ultrasonic treatment $\text{Bi}_2\text{O}_2\text{CO}_3$ in the KI solution exhibit much higher photocatalytic activity than the single $\text{Bi}_2\text{O}_2\text{CO}_3$ and BiOI for the degradation of RhB under visible light irradiation. The BiOI/ $\text{Bi}_2\text{O}_2\text{CO}_3$ heterostructures obtained with ultrasonic reaction for 45 min shows the best photocatalytic activity. The enhanced photocatalytic performance is suggested to be related to the p–n junction between n-type $\text{Bi}_2\text{O}_2\text{CO}_3$ and p-type BiOI, which is regarded to be favorable for the separation of photogenerated electrons and holes. Moreover, photocatalytic mechanism investigations demonstrate that h^+ and O_2^- play the key role in the BiOI/ $\text{Bi}_2\text{O}_2\text{CO}_3$ heterostructures under visible light illumination. The resulting BiOI/ $\text{Bi}_2\text{O}_2\text{CO}_3$ heterostructures may be a promising efficient photocatalyst for degradation organic pollutants.

Acknowledgments This work was supported by Science and Technology Investigation Project of Educational Committee of Hubei Province, China (No. Q20141708).

References

- X.L. Hu, G.S. Li, J.C. Yu, *Langmuir* **26**, 3031 (2010)
- A. Kubacka, M. Fernández-García, G. Colón, *Chem. Rev.* **112**, 1555 (2012)
- H. Wang, J. Gao, T.Q. Guo, R.M. Wang, L. Guo, Y. Liu, J.H. Li, *Chem. Commun.* **48**, 275 (2012)
- Y.P. Bi, S.X. Ouyang, N. Umezawa, J.Y. Cao, J.H. Ye, *J. Am. Chem. Soc.* **133**, 6490 (2011)
- G.P. Dai, J.G. Yu, G. Liu, *J. Phys. Chem. C* **116**, 15519 (2012)
- G.C. Xi, J.H. Ye, *Chem. Commun.* **46**, 1893 (2010)
- G.H. Tian, Y.J. Chen, W. Zhou, K. Pan, Y.Z. Dong, C.G. Tian, H.G. Fu, *J. Mater. Chem.* **21**, 887 (2011)
- M. Shang, W.Z. Wang, S.M. Sun, L. Zhou, L. Zhang, *J. Phys. Chem. C* **112**, 10407 (2008)
- B. Chai, H. Zhou, F. Zhang, X. Liao, M.X. Ren, *Mater. Sci. Semicond. Process.* **23**, 151 (2014)
- X. Xiao, W.D. Zhang, *J. Mater. Chem.* **20**, 5866 (2010)
- G.G. Zhang, J.S. Zhang, M.W. Zhang, X.C. Wang, *J. Mater. Chem.* **22**, 8083 (2012)
- G.H. Tian, Y.J. Chen, H.L. Bao, X.Y. Meng, K. Pan, W. Zhou, C.G. Tian, J.Q. Wang, H.G. Fu, *J. Mater. Chem.* **22**, 2081 (2012)
- S. Kumar, T. Surendar, A. Baruah, V. Shanker, *J. Mater. Chem. A* **1**, 5333 (2013)

14. W.Z. Wang, X.W. Huang, S. Wu, Y.X. Zhou, L.J. Wang, H.L. Shi, Y.J. Liang, B. Zou, *Appl. Catal. B: Environ.* **134–135**, 293 (2013)
15. M.Y. Zhang, C.L. Shao, J.B. Mu, Z.Y. Zhang, Z.C. Guo, P. Zhang, Y.C. Liu, *CrystEngComm* **14**, 605 (2012)
16. H.F. Cheng, B.B. Huang, P. Wang, Z.Y. Wang, Z.Z. Lou, J.P. Wang, X.Y. Qin, X.Y. Zhang, Y. Dai, *Chem. Commun.* **47**, 7054 (2011)
17. J. Cao, B.Y. Xu, B.D. Luo, H.L. Lin, S.F. Chen, *Catal. Commun.* **13**, 63 (2011)
18. T.Y. Zhao, J.T. Zai, M. Xu, Q. Zou, Y.Z. Su, K.X. Wang, X.F. Qian, *CrystEngComm* **13**, 4010 (2011)
19. H.F. Cheng, B.B. Huang, K.S. Yang, Z.Y. Wang, X.Y. Qin, X.Y. Zhang, Y. Dai, *ChemPhysChem* **11**, 2167 (2010)
20. X.F. Chang, J. Huang, C. Cheng, Q. Sui, W. Sha, G.B. Ji, S.B. Deng, G. Yu, *Catal. Commun.* **11**, 460 (2010)
21. X. Zhang, Z.H. Ai, F.L. Jia, L.Z. Zhang, *J. Phys. Chem. C* **112**, 747 (2008)
22. P. Madhusudan, J.R. Ran, J. Zhang, J.G. Yu, G. Liu, *Appl. Catal. B: Environ.* **110**, 286 (2011)
23. X.W. Huang, H.F. Chen, *Appl. Surf. Sci.* **284**, 843 (2013)
24. Y.S. Xu, W.D. Zhang, *Appl. Catal. B: Environ.* **140–141**, 306 (2013)
25. N. Liang, J.T. Zai, M. Xu, Q. Zhu, X. Wei, X.F. Qian, *J. Mater. Chem. A* **2**, 4208 (2014)
26. M. Xiong, L. Chen, Q. Yuan, J. He, S.L. Luo, C.T. Au, S.F. Yin, *Dalton Trans.* **43**, 8331 (2014)
27. G.Y. Cai, L.L. Xu, B. Wei, J.X. Che, H. Gao, W.J. Sun, *Mater. Lett.* **120**, 1 (2014)
28. G.P. Dai, J.G. Yu, G. Liu, *J. Phys. Chem. C* **115**, 7339 (2011)
29. J. Jiang, X. Zhang, P.B. Sun, L.Z. Zhang, *J. Phys. Chem. C* **115**, 20555 (2011)
30. J. Cao, X. Li, H.L. Lin, S.F. Chen, X.L. Fu, *J. Hazard Mater.* **239–240**, 316 (2012)
31. L. Chen, S.F. Yin, S.L. Luo, R. Huang, Q. Zhang, T. Hong, P.C.T. Au, *Ind. Eng. Chem. Res.* **51**, 6760 (2012)
32. F. Dong, Y.J. Sun, M. Fu, W.K. Ho, S.C. Lee, Z.B. Wu, *Langmuir* **28**, 766 (2012)